Journal of Advanced Ceramics
2022, **11**(8): 1187–1195
https://doi.org/10.1007/s40145-022-0592-4
ISSN 2226-4108
CN 10-1154/TQ

Research Article

Controllable growth of single-crystalline zinc oxide nanosheets under ambient condition toward ammonia sensing with ultrahigh selectivity and sensitivity

Dongdong ZHANG[a,b], Zhi FANG[b], Lin WANG[b], Hao YU[a,b], Xianlu LU[a,b], Kai SONG[b], Jie TENG[a,*], Weiyou YANG[b,*]

[a]*College of Materials Science and Engineering*, *Hunan University*, *Changsha 410082*, *China*
[b]*Institute of Micro/Nano Materials and Devices*, *Ningbo University of Technology*, *Ningbo 315211*, *China*

Received: February 22, 2022; Revised: March 19, 2022; Accepted: March 26, 2022

Abstract: To date, the synthesis of crystalline ZnO nanostructures was often performed under high temperatures and/or high pressures with tiny output, which limits their commercial applications. Herein, we report the progress on synthesizing single-crystalline ZnO nanosheets under ambient conditions (i.e., room temperature (RT) and atmospheric pressure) based on a sonochemistry strategy. Furthermore, their controllable growth is accomplished by adjusting the pH values of solutions, enabling the tailored crystal growth habits on the polar-charged faces of ZnO along *c*-axis. As a proof of concept for their potential applications, the ZnO nanosheets exhibit highly efficient performance for sensing ammonia at RT, with ultrahigh sensitivity (S = 610 at 100 ppm), excellent selectivity, rapid detection (response time/recover time = 70 s/4 s), and outstanding detection limit down to 0.5 ppm, superior to those of all pure ZnO nanostructures and most ZnO-based composite counterparts ever reported. The present work might open a door for controllable production of ZnO nanostructures under mild conditions, and facilitate the exploration of modern gas sensors for detecting gaseous molecules at RT, which underscores their potential toward practical applications in opto-electronic nanodevices.

Keywords: zinc oxide (ZnO); nanostructures; ambient condition; crystal growth; gas sensor

1 Introduction

Zinc oxide (ZnO) is recognized as one of the most important third-generation semiconductors with versatilely excellent performances, such as high electron mobility, direct wide band-gap (3.37 eV), large exciton binding energy (60 MeV) at room temperature (RT) [1,2], as well as high mechanical and thermal stabilities, which has interesting applications in high-efficiency short-wavelength optoelectronic devices [3,4]. Moreover, the unique piezo and pyroelectric properties allow it to be used in piezoelectric sensors [5], energy harvesting devices [6,7], etc. Additionally, the intrinsically low toxicity, biocompatibility, and biodegradability merits make it a potential candidate to be serviced in biomedicine and inpro-ecological systems [8,9].

* Corresponding authors.
E-mail: J. Teng, tengjie@hnu.edu.cn;
W. Yang, weiyouyang@tsinghua.org.cn

In comparison to conventional bulk counterparts, the nanomaterials exhibit superior physical/chemical performances with exciting applications in modern nanodevices. For rationally designed growth of ZnO nanostructures, a wide range of techniques were progressed, such as the aqueous solution method [10,11], physical vapor deposition [12,13], metal–organic chemical vapor deposition [14,15], electrodeposition [16,17], and etching [18]. However, most of the reported works concerning on growing ZnO nanostructures encounter two grand challenges: One is their tiny output with also time-consuming process, and the other is that their growth had to be performed under the assistance of high temperatures and/or high pressures. That is to say, the fabrication of ZnO nanostructures under mild conditions is highly desired, which is one of the critical and important points to push forward their practical applications.

In terms of the shape-dependent performance of nanostructures, to date, numerous efforts have been put for growing ZnO nanostructures with fruitful morphologies, typically including nanowires [19], nanorods [10,20], nanobelts [12,21], nanorings [15,21], etc. [15,22]. Amongst, the sheet-like configurations have attracted numerous attentions, due to its unique high surface areas with large-exposed crystal facets and excellent charge-transport characteristics, thus delivering great potential to be applied in opto-electronic devices [23–25]. Unfortunately, as compared to the analogues such as nanowires, the growth of ZnO two-dimensional (2D)-like nanosheets is much more difficult, which might be attributed to its intrinsically hexagonal polar structure. In such circumstance, the basal plane of (0001) has the highest surface energy, thus always inducing the fast growth along *c*-axis direction for preferred formation of one-dimensional (1D) nanowire [22,26]. Herein, we report the progress for fabricating single-crystalline ZnO nanostructures based on a sonochemical route under ambient condition. Furthermore, their controlled growth has been accomplished by the tailored pH values based on adjusting the compositions of reactant solvents. Particularly, as compared to the nanorod counterpart, the as-synthesized ZnO nanosheets exhibit an overall enhanced activity for sensing NH_3 gas at RT with ultrahigh selectivity and sensitivity, representing their bright future toward practical applications.

2 Experimental

2. 1 Reagents

Zinc (Zn) (99.9%, 40–50 nm) powders were purchased from Titd Metal Material Co., Ltd. Hydrochloric acid (HCl) (roughly 36%–38%) and ethanediamine (EDA) ($\geqslant$ 99.0%) were purchased from Sinopharm Chemical Reagent Co., Ltd. The deionized water (DIW) was used in all experiments. All reagents were used as received without further purification.

2. 2 Synthesis of ZnO nanosheets

In a typical process, 1 mmol Zn powders were added into 15 mL of 0.5 M HCl to form an even suspension solution under stirring at a speed of 400 r/min, followed by an ultrasonic treatment at a frequency of 40 kHz for 4 h. The resultant products were collected by the centrifugation of 5 min, and washed with DIW three times. Finally, the obtained precipitates were dried under ambient condition.

2. 3 Synthesis of ZnO nanorods

In a typical process, 1 mmol Zn powders were added into 13 mL of DIW and 2 mL EDA to form an even suspension solution under stirring at a speed of 400 r/min, followed by an ultrasonic treatment at a frequency of 40 kHz for 4 h. The resultant products were collected by the centrifugation for 5 min, and washed with H_2O three times. Finally, the obtained precipitates were dried under ambient condition.

2. 4 Characterizations

The powder X-ray diffractometer (D8 Advance, Bruker, Germany) with a Cu Kα X-ray radiation (λ = 1.5406 Å) and the Raman spectrometer (Raman, Renishaw inVia, UK) with an excitation laser of 532 nm were utilized to evaluate the phase compositions. The microstructures and morphologies of the as-prepared samples were observed under a field emission scanning electron microscope (FESEM; S-4800, Hitachi, Japan) and a high-resolution transmission electron microscope (HRTEM; JEM-2100F, JEOL, Japan) equipped with an energy dispersive X-ray (EDX) spectroscope (Quantax-STEM, Bruker, Germany). The compositions and valence band of the product were analyzed by the X-ray photoelectron spectroscope (XPS; Scientific K-Alpha, Thermo, USA) with a reference of C 1s peak

at 284.6 eV. The ultraviolet–visible (UV–Vis) absorption spectrum was recorded on a UV–Vis scanning spectrophotometer (U-3900, Hitachi, Japan). The porous properties of as-prepared ZnO nanostructures were characterized using N_2 adsorption at 77 K on a specific surface area and porosity analyzer (Micromeritics, ASAP 2020M, USA).

2. 5 Gas-sensing test

To fabricate an interdigitated electrode (IDE), the Au electrodes with a typical thickness in ~50 nm were deposited on the polyethylene terephthalate (PET) substrate (15 mm × 15 mm) by photo lithography, and then subjected to thermal evaporation treatment. This allowed the preparation of interdigital patterns sized in 10 mm × 10 mm, in which the channel width between two adjacent electrodes was typically fixed in ~100 μm with a total of 15 pairs. After that, the as-prepared ZnO nanosheets were mixed with ethanol, followed by ultrasonic dispersion to form an emulsion, which was then coated on the as-fabricated IDE. For enhancing the contact between the ZnO nanosheets and electrode, the devices were dried at 80 ℃ for ~10 min. To show the selectivity for gas sensing, eight kinds of volatile organic molecule gases were chosen as interfering species, including toluene (C_7H_8), methanol (CH_3OH), acetone (CH_3COCH_3), ethanol (CH_3CH_2OH), ammonia (NH_3), chloroform ($CHCl_3$), acetic acid (CH_3COOH), and acetaldehyde (CH_3CHO).

3 Results and discussion

Figure 1(a) schematically illustrates the production of ZnO nanostructures with Zn powders as source materials under ambient condition based on the sonochemistry strategy (the details are shown in Section 2). In a typical process, 15 mL 0.5 M HCl solution with 1 mmol Zn nanoparticles is mixed under agitation, followed by an ultrasonic treatment for 4 h at a frequency of 40 kHz under ambient condition. Figures 1(b) and 1(c) disclose that the as-synthesized ZnO nanostructures are sheet-like with hexagon lateral dimensions typically sized in 0.5–1.5 μm, which is a statistical analysis based on the SEM observation as shown in Fig. 1(b). The recorded TEM image clarifies that they have smooth surfaces and clearly-defined edges (Fig. 1(d)). Both the HRTEM image and corresponding lattice Fourier transform pattern (the up-right inset in Fig. 1(e)) reveal its single-crystalline nature with a large-exposed crystal facet of (0001) [27] (see the selected area electron diffraction (SAED) in Fig. S1 in the Electronic Supplementary Material (ESM)). The enlarged HRTEM image (the down-left inset in Fig. 1(e)) presents the *d*-spacing of 0.28 nm, corresponding to the (100) planes of ZnO. Figure 1(f) provides the typical X-ray diffraction (XRD) pattern, further confirming that they are pure-phase hexagonal wurtzite ZnO (JCPDS Card No. 36-1451). Figure 1(g) shows a Raman spectrum of ZnO nanosheets excited with a laser at 532 nm. All the observed spectroscopic peaks can be assigned to the wurzite ZnO [28]. Furthermore, the characterizations such as XPS (Fig. S2 in the ESM) and UV–Vis absorption spectroscopy (Fig. S3 in the ESM) verify their wurtzite phase (see the details in Figs. S2 and S3 in the ESM). Significantly, the present work is distinctively different and superior to most of the works ever reported (Table S1 in the ESM), which had to be performed under externally applied high temperatures and/or high pressures. Furthermore, to show the detailed growth of ZnO nanosheets, the products are observed at given sonication time from 1, 2 to 4 h, as shown in Fig. S4 in the ESM. It seems that at a sonication time of 1 h, the precursors of Zn nanoparticles are melted, accompanying by the formation of numerous ZnO nanoparticles (Fig. S4(a) and S4(b) in the ESM). Once the sonication time is extended to 2 h, the small and thin ZnO nanosheets could be representatively formed (Figs. S4(c) and S4(d) in the ESM). Once the sonication time is further raised up to 4 h, the growth of ZnO nanosheets is accomplished (Figs. S4(e) and S4(f) in the ESM). Briefly, the growth of ZnO nanosheets under sonication treatment mainly involves two typical steps, which concludes the *in-situ* nucleation of ZnO crystals (Step 1 in Fig. 1(h)), followed by the growth of ZnO nanosheets (Step 2 in Fig. 1(h)).

To enable the growth of ZnO nanostructures with elaborated morphologies, the key experimental parameters of used solvents are adjusted, by using H_2O+EDA instead of HCl. Figure S5(a) in the ESM schematically illustrates the growth of ZnO nanostructures via a sonochemical method using H_2O+EDA as the solvent with otherwise similar conditions. Their detailed growth is also observed at given sonication time from 1, 3 to 4 h, as shown in Figs. S5(b)–S5(d) in the ESM, suggesting that it also involves two typical steps like to those of nanosheet (Fig. S5(a) in the ESM). Figures 2(a)

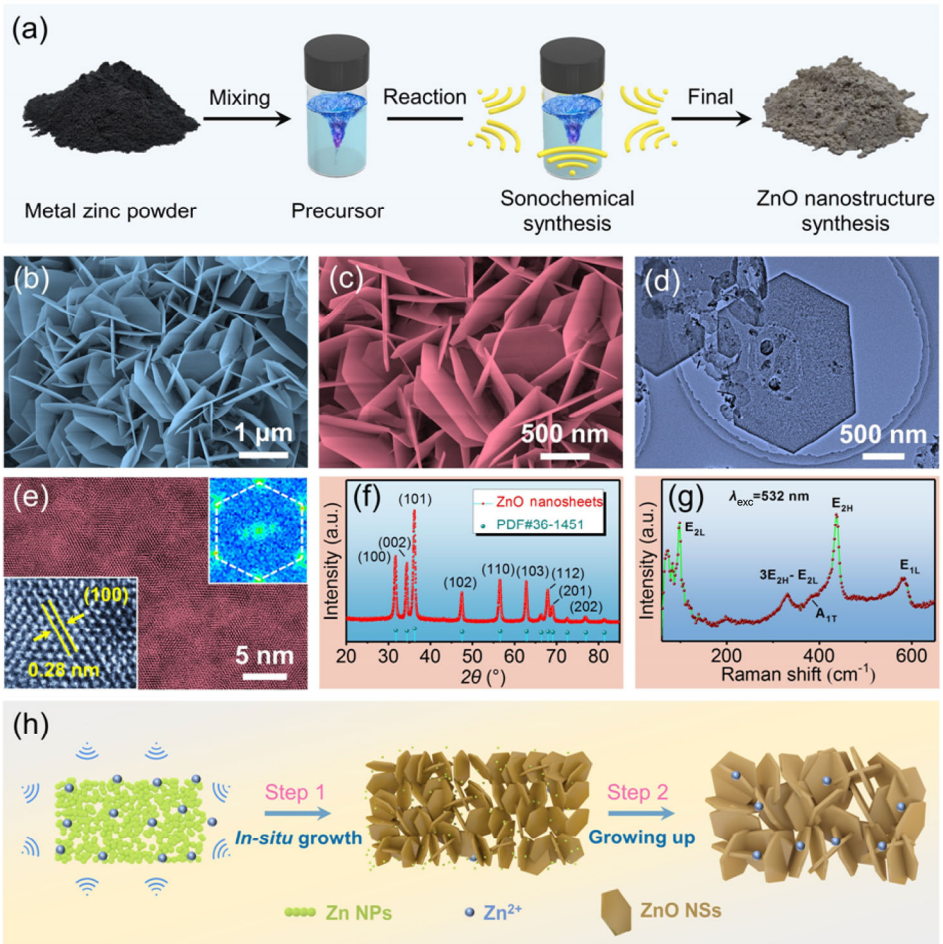

Fig. 1 Characterizations of ZnO nanosheets. (a) Schematic illustration on growing ZnO nanostructures under ultrasonic treatment. (b, c) Representative SEM images of resultant ZnO nanosheets under different magnifications. (d, e) Typical TEM and HRTEM images of ZnO nanosheets, respectively. The down-left and up-right insets in (e) are the lattice fringes and fast Fourier transitions, respectively. (f) Typical XRD pattern of ZnO nanosheets. (g) Typical Raman spectrum of ZnO nanosheets excited at λ_{exc} = 532 nm. (h) Schematic illustration on the growth of ZnO nanosheets under continuous ultrasonic treatment.

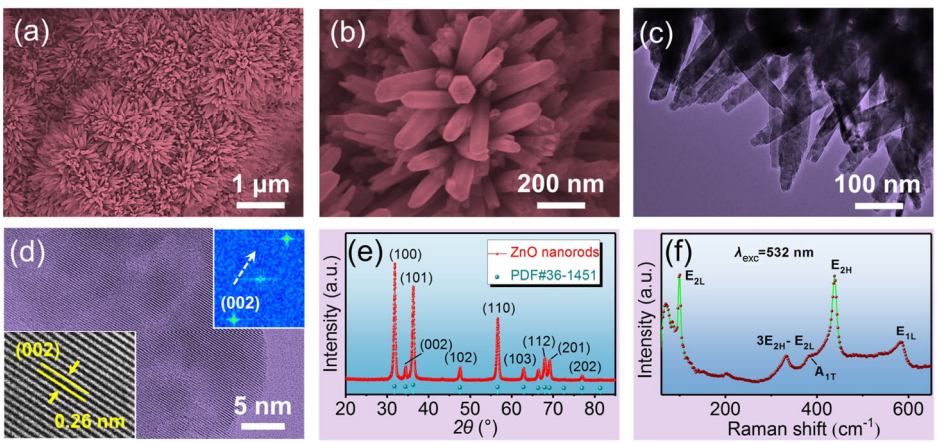

Fig. 2 Characterizations of ZnO nanorods. (a, b) Representative SEM images of resultant ZnO nanorods under different magnifications. (c, d) Typical TEM and HRTEM images of ZnO nanorods, respectively. The down-left and up-right insets in (d) are the lattice fringes and fast Fourier transitions, respectively. (e) Typical XRD pattern of ZnO nanorods. (f) Typical Raman spectrum of ZnO nanorods excited at λ_{exc} = 532 nm.

and 2(b) present the typical SEM images of as-grown ZnO nanorods under different magnifications, which are fabricated based on a reaction solvent with a volume ratio of H_2O:EDA = 13:2 and a sonication time of 4 h. The as-prepared ZnO nanorods are arranged in bushlike assembly with a diameter and mean length of 20–50 nm and 1 μm, respectively. The TEM image (Fig. 2(c)), HRTEM image (Fig. 2(d)), and corresponding lattice Fourier transform pattern (the up-right inset in Fig. 2(d)) reveal its single-crystalline nature with a preferential [0001] growth direction. The enlarged HRTEM image (the down-left inset in Fig. 2(d)) presents the *d*-spacing of 0.26 nm, corresponding to the (002) planes of ZnO. Figure 2(e) provides the typical XRD pattern, further confirming their pure-phase hexagonal wurtzite ZnO (also see the SAED in Fig. S6 in the ESM) (JCPDS Card No. 36-1451). Furthermore, the characterizations such as the Raman spectrum (Fig. 2(f)), XPS (Fig. S7 in the ESM) and UV–Vis absorption spectroscopy (Fig. S8 in the ESM) verify that they are ZnO in pure wurtzite phase.

Then we come to a point about the mechanism on the controlled growth of ZnO nanosheets, as shown in Fig. 3. Over the growth of ZnO nanostructures in various environments of HCl and H_2O+EDA solutions, the possible main reactions are presented in Fig. 3(a). As we know, the ZnO crystal holds the unique feature of polar-charged faces along *c*-axis, which has chemically active Zn-terminated (0001) planes and inert O-terminated ($000\bar{1}$) ones [22,26]. For the growth of ZnO nanosheets, once HCl is introduced in the aqueous solution, the H^+ ions instead of OH^- ones would be dominant, which prefers to contact with O^{2-} terminated plane (Step 1 in Fig. 3(b)), due to the stronger O–H

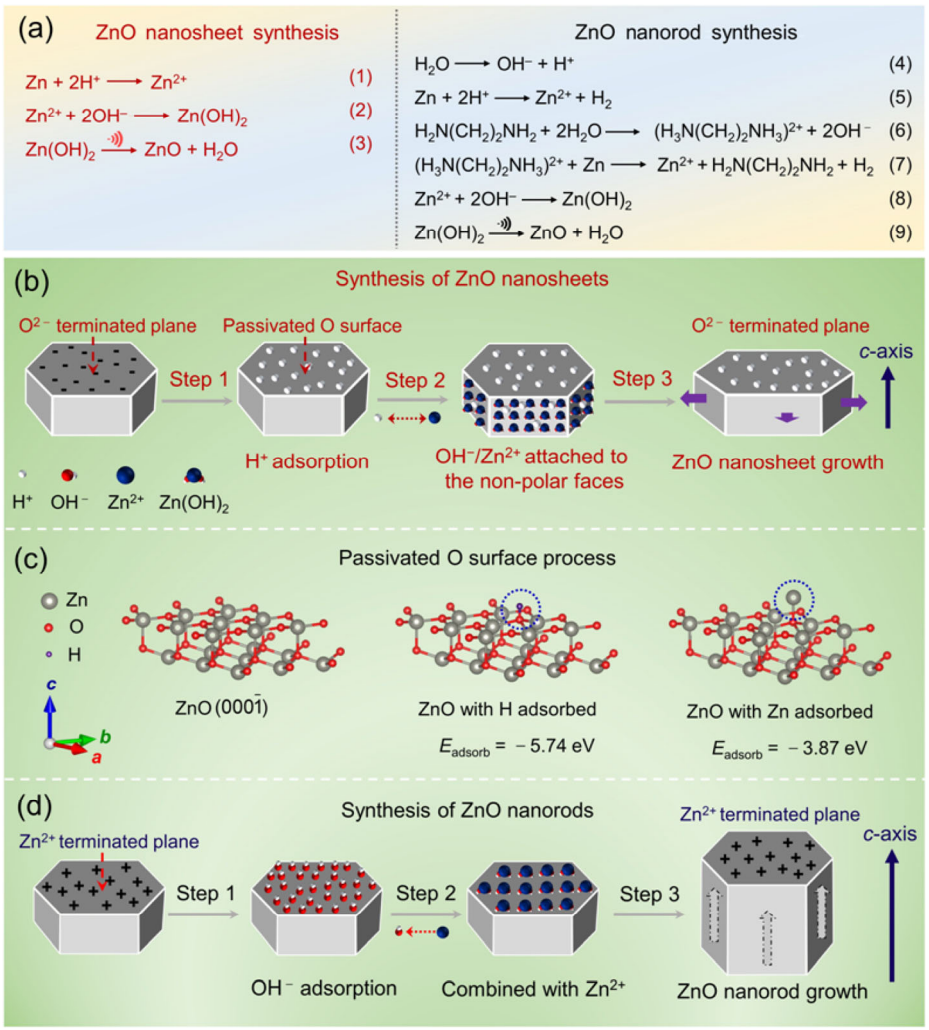

Fig. 3 Growth mechanism. (a) Equations involved in the growth of ZnO nanorods and nanosheets. (b) Schematic illustration on the growth of ZnO nanosheets. (c) Surface adsorption energies of ZnO ($000\bar{1}$) facets with adsorbed H and Zn atoms. (d) Schematic illustration on the growth of ZnO nanorods.

bonds compared with O–Zn ones. This could be confirmed by the calculated energies of O–H and Zn–O bonds on O^{2-} terminated plane, which are −5.74 and −3.87 eV, respectively, as shown in Fig. 3(c) and Fig. S9 in the ESM. That is to say, in such case, the growth of ZnO crystals along Zn-terminated (0001) plane would be hindered. Accordingly, the OH^- ions would be driven to bond Zn^{2+} ions within non-polar faces for generating $Zn(OH)_2$, thus making the growth of ZnO crystals along radical direction rather than *c*-axis (Reactions (1)–(3) in Fig. 3(a)), and accounting for the formation of ZnO nanosheets (Step 3 in Fig. 3(b)). To confirm the passive effect of H^+ on the crystal growth on polar-charged faces of ZnO, the comparison experiment is carried out, in which the concentration of introduced HCl is reduced from 0.5 M (Fig. 3(b)) to 0.2 M (Fig. S10 in the ESM), with otherwise similar conditions. It represents that the as-grown ZnO nanosheets become much thicker, verifying the limited growth of ZnO crystals along *c*-axis direction induced by H^+ ions. As for growing ZnO nanorods, over the beginning of the process, the metal Zn would be oxidized into Zn^{2+} ions by H^+, which comes from the decomposition of H_2O and $(H_3N(CH_2)_2NH_3)^{2+}$ (derived from the hydrolysis of EDA (Reactions (4)–(7) in Fig. 3(a)). Subsequently, the Zn^{2+} would react with OH^- for the formation of $Zn(OH)_2$, leading to the nucleation of ZnO under ultrasonic treatment (Reactions (8) and (9) in Fig. 3(a)). Over the following crystal growth, the Zn^{2+} in Zn-terminated (0001) plane would be coordinated with OH^- ions within the solution (Step 1 in Fig. 3(d)) driven by the electrostatic attraction for generating $Zn(OH)_2$ (Step 2 in Fig. 3(d) and Reaction (8) in Fig. 3(a)), followed by the dehydration for the formation of ZnO (Step 3 in Fig. 3(d) and Reaction (9) in Fig. 3(a)). Especially, numerous OH^- ions generated by the hydrolysis of EDA (Reaction (6) in Fig. 3(a)) would be attracted to Zn-terminated (0001) plane (Reaction (8) in Fig. 3(a)), thus facilitating the fast growth along *c*-axis to favor the growth of nanorods. Briefly, based on the rationally-designed solutions, the controllable growth of ZnO nanosheets could be accomplished.

To show the application of ZnO nanosheets, the gas-sensing device is constructed, as schematically illustrated in Figs. 4(a) and 4(b). Figure 4(c) gives its responses to NH_3 gases with different concentrations of 1, 5, 10, 20, 50, 100, 200, and 500 ppm, which are of 4, 8, 83, 186, 230, 610, 639, and 690, respectively (also see Table S3 in the ESM). Moreover, the fitted curve of sensing response vs. NH_3 gas concentration in the range of 1–500 ppm is provided. It seems that the correlation coefficient R^2 over the range of 1–100 ppm is ~0.95, and that over the range of 100–500 ppm is ~0.96, indicating the good linearity in both cases (Fig. S11 in the ESM). Notably, the response of 610 of ZnO nanosheets is much better than that of ZnO nanorods (S = 40 at 100 ppm, as shown in Fig. S12 in the ESM), which could be ascribed to their much higher surface areas with fully exposed active sites (Fig. S13 in the ESM). Interestingly, the limit detection could be low to 0.5 ppm (the inset in Fig. 4(d)), witnessing its high sensitivity for NH_3 detection. Furthermore, the device delivers an excellent cycling performance (Fig. 4(d)) with reproducible capability. The response and recovery time (defined as the time to reach 70% of total resistance change) at 100 ppm NH_3 are ~70 and ~4 s, respectively (Fig. 4(f)), verifying its capacity for rapid detection. It should be pointed out that the overall NH_3 sensing performances are superior to those of all pure ZnO nanostructures and most ZnO-based composite counterparts ever reported (Fig. 4(e) and Table S2 in the ESM). Figure 4(g) provides the schematic illustration on the gas-sensing mechanism, based on two various environments in air and NH_3. Once ZnO nanosheets are exposed to air, the oxygen would be adsorbed on the surface, resulting in the trap of electrons from the conduction band of ZnO, accompanying by the formation of oxygen species (O^- or O^{2-}), agreeing on the experimental XPS analyses (Fig. S2 in the ESM). Correspondingly, the width of space charge region would be enlarged with the raised height of potential barrier. However, once in reducing atmosphere, the introduced NH_3 would react with the adsorbed oxygen species (O^- or O^{2-}), causing the release of trapped electrons. This would in-turn decrease the width of space charge region with increased surface conductivity of ZnO nanosheets, thus responding to the changed resistances. The higher concentration of NH_3, the more released electrons would happen to reduce the resistance, as shown by the experimental responses to different concentrations in Fig. 4(c).

Figure 4(h) presents the selectivity for sensing NH_3 by being exposed to eight kinds of various gases, including toluene (C_7H_8), methanol (CH_3OH), acetone (CH_3COCH_3), ethanol (CH_3CH_2OH), ammonia (NH_3),

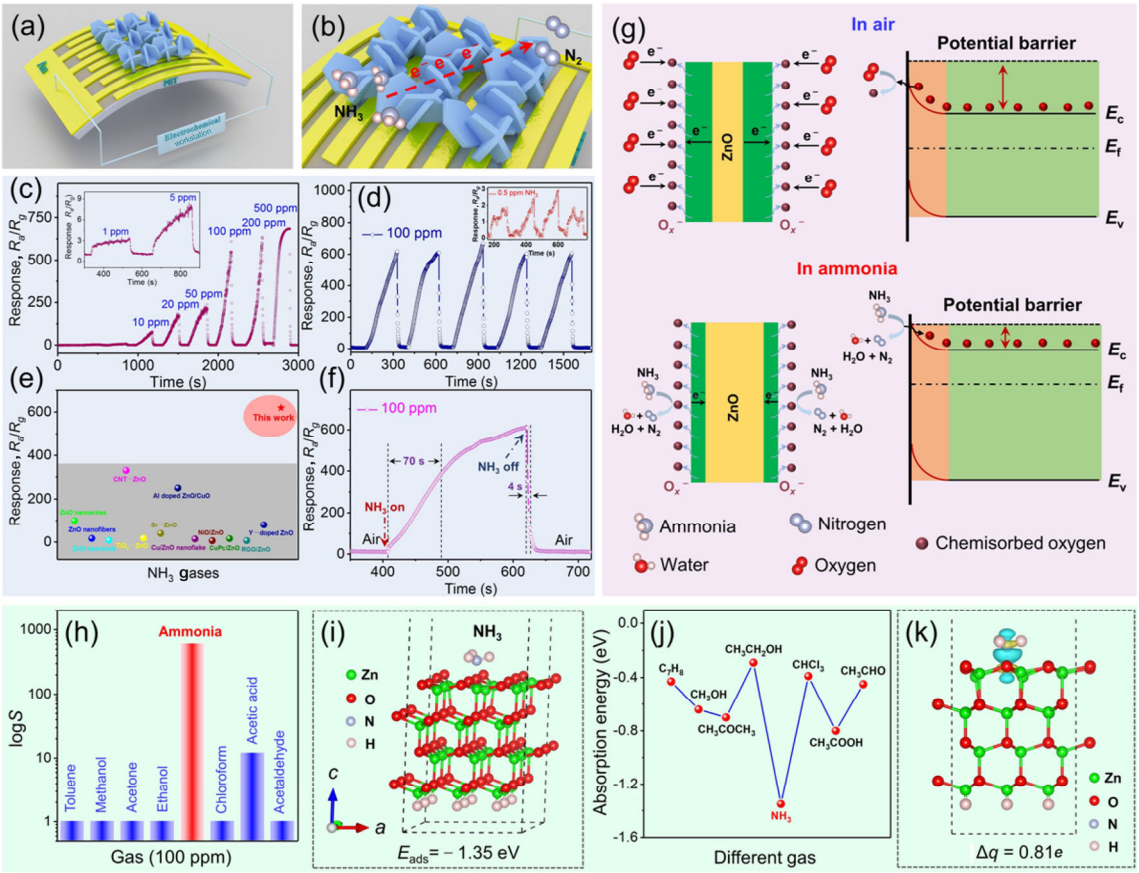

Fig. 4 Gas-sensing performance and mechanism. (a, b) Schematic illustrations on constructing gas sensor based on ZnO nanosheets. (c) Response–recovery curves of the sensor responding to NH_3 with different concentrations at RT. (d) Cycling performance of the sensor to 100 ppm NH_3 at RT. The inset shows its response to 0.5 ppm NH_3. (e) Typical responses of pure ZnO nanostructures and ZnO-based composite counterparts for sensing NH_3 at RT ever reported (Table S2 in the ESM). (f) Response and recovery time of the sensor exposed to 100 ppm NH_3. (g) Schematically illustrated mechanism for sensing NH_3 based on ZnO nanosheets. (h) Selectivity for sensing NH_3 in 100 ppm at RT. (i) Calculated surface adsorption energies of ZnO $(000\bar{1})$ facets with adsorbed NH_3. (j) Adsorption energies of eight kinds of gases on ZnO nanosheets. (k) Calculated charge density difference of ZnO nanosheets after NH_3 adsorption.

chloroform ($CHCl_3$), acetic acid (CH_3COOH), and acetaldehyde (CH_3CHO). It seems that the response value for NH_3 (S = 610 at 100 ppm) is at least 50 times as high as those of the other interfering ones (i.e., that of acetic acid is S = 12 at 100 ppm, and those of others have nearly no response, also see Table S4 in the ESM). The excellent selectivity could be mainly attributed to the higher adsorption capacity and stronger reducibility of NH_3 molecules on ZnO nanosheet surface with large-exposed crystal facet of (0001), which could facilitate the reaction rate and electron transfer at RT in comparison to the other gases. To understand the selective gas-sensing process, theoretical investigations based on density functional theory (DFT) are performed. Over the initial process, the $(000\bar{1})$ facets of ZnO slabs adsorbed by NH_3 molecular are simulated, based on the recorded HRTEM and fast Fourier transform pattern (Fig. 1(e)). It discloses that the sensor exhibits the highest adsorption energies E_{ads} of −1.35 eV over NH_3 among the given eight kinds of gases (Fig. 4(i) and Fig. S14 in the ESM), in consistence with the experimental results (Fig. 4(h)). All the E_{ads} values are less than 2.0 eV, indicating the physically-adsorbed process of all gases on ZnO nanosheets (Fig. 4(j)) [29]. Moreover, the charge densities are calculated to evaluate the electron transfer during the NH_3 sensing process (Fig. 4(k)), clarifying that there is 0.81e of electron transferred from NH_3 to ZnO. Briefly, the fundamentally enhanced gas-sensing performance could be mainly attributed to the abundant active sites for NH_3 adsorption

and accelerated electronic transfer enabled by the single-crystalline nature of ZnO nanosheets with large-exposed crystal facet of (0001).

4 Conclusions

In summary, we report a facile and efficient sonochemistry strategy for fabricating single-crystalline ZnO nanosheets under ambient condition. Their controlled growth has been accomplished by adjusting the pH values of solutions, based on the intrinsic feature of ZnO crystals with unique polar-charged faces along *c*-axis. The as-constructed gas sensor exhibits highly efficient performance for sensing NH_3 at RT, which has an ultrahigh sensitivity (S = 610 at 100 ppm), excellent selectivity, rapid detection (response time/recover time = 70 s/4 s), and outstanding detection limit (S = 2 at 0.5 ppm) as well as excellent reversibility, which are superior to those of all pure ZnO nanostructures and most ZnO-based composite counterparts ever reported. The totally-enhanced NH_3 gas sensing performance could be mainly attributed to the unique single-crystalline nature of as-synthesized ZnO nanosheets, which could not only endow enough exposed active sites responding to the NH_3, but also provide fast pathway for efficient transfer of carriers. In terms of their controllable fabrication under mild conditions as well as their high physical performance, current work might be meaningful to push forward the commercial applications of ZnO nanostructures in the advanced opto/electronic nanodevices.

Acknowledgements

This work was supported by the National Natural Science Foundation of China (Grant No. 51972178) and Hunan Provincial Innovation Foundation for Postgraduate (Grant No. CX20200454).

Declaration of competing interest

The authors have no competing interests to declare that are relevant to the content of this article.

Electronic Supplementary Material

Supplementary material is available in the online version of this article at https://doi.org/10.1007/s40145-022-0592-4.

References

[1] Zhang QF, Dandeneau CS, Zhou XY, e*t al*. ZnO nanostructures for dye-sensitized solar cells. *Adv Mater* 2009, **21**: 4087–4108.
[2] Sowri Babu K, Ramachandra Reddy A, Sujatha C, *et al*. Synthesis and optical characterization of porous ZnO. *J Adv Ceram* 2013, **2**: 260–265.
[3] Huang MH, Mao S, Feick H, *et al*. Room-temperature ultraviolet nanowire nanolasers. *Science* 2001, **292**: 1897–1899.
[4] Park WI, Yi GC. Electroluminescence in n-ZnO nanorod arrays vertically grown on p-GaN. *Adv Mater* 2004, **16**: 87–90.
[5] Wei TY, Yeh PH, Lu SY, *et al*. Gigantic enhancement in sensitivity using schottky contacted nanowire nanosensor. *J Am Chem Soc* 2009, **131**: 17690–17695.
[6] Wang ZL, Song JH. Piezoelectric nanogenerators based on zinc oxide nanowire arrays. *Science* 2006, **312**: 242–246.
[7] Wang ZL. The new field of nanopiezotronics. *Mater Today* 2007, **10**: 20–28.
[8] Siebert L, Luna-Cerón E, García-Rivera LE, *et al*. Light-controlled growth factors release on tetrapodal ZnO-incorporated 3D-printed hydrogels for developing smart wound scaffold. *Adv Funct Mater* 2021, **31**: 2007555.
[9] Zheng G, Patolsky F, Cui Y, *et al*. Multiplexed electrical detection of cancer markers with nanowire sensor arrays. *Nat Biotechnol* 2005, **23**: 1294–1301.
[10] Vayssieres L. Growth of arrayed nanorods and nanowires of ZnO from aqueous solutions. *Adv Mater* 2003, **15**: 464–466.
[11] Liu B, Zeng HC. Hydrothermal synthesis of ZnO nanorods in the diameter regime of 50 nm. *J Am Chem Soc* 2003, **125**: 4430–4431.
[12] Pan ZW, Dai ZR, Wang ZL. Nanobelts of semiconducting oxides. *Science* 2001, **291**: 1947–1949.
[13] Huang MH, Wu Y, Feick H, *et al*. Catalytic growth of zinc oxide nanowires by vapor transport. *Adv Mate*r 2001, **13**: 113–116.
[14] Park WI, Yi GC, Kim M, *et al*. ZnO nanoneedles grown vertically on Si substrates by non-catalytic vapor-phase epitaxy. *Adv Mater* 2002, **14**: 1841–1843.
[15] Hughes WL, Wang ZL. Formation of piezoelectric single-crystal nanorings and nanobows. *J Am Chem Soc* 2004, **126**: 6703–6709.
[16] Li Y, Meng GW, Zhang LD, *et al*. Ordered semiconductor ZnO nanowire arrays and their photoluminescence properties. *Appl Phys Lett* 2000, **76**: 2011–2013.
[17] Anthony SP, Lee JI, Kim JK. Tuning optical band gap of vertically aligned ZnO nanowire arrays grown by homoepitaxial electrodeposition. *Appl Phys Lett* 2007, **90**: 103107.
[18] Wu JJ, Wen HI, Tseng CH, *et al*. Well-aligned ZnO nanorods

via hydrogen treatment of ZnO films. *Adv Funct Mater* 2004, **14**: 806–810.

[19] Nikoobakht B, Wang XD, Herzing A, *et al*. Scalable synthesis and device integration of self-registered one-dimensional zinc oxide nanostructures and related materials. *Chem Soc Rev* 2013, **42**: 342–365.

[20] Wu JJ, Liu SC. Low-temperature growth of well-aligned ZnO nanorods by chemical vapor deposition. *Adv Mater* 2002, **14**: 215–218.

[21] Kong XY, Ding Y, Yang RS, *et al*. Single-crystal nanorings formed by epitaxial self-coiling of polar nanobelts. *Science* 2004, **303**: 1348–1351.

[22] Wang ZL, Kong XY, Zuo JM. Induced growth of asymmetric nanocantilever arrays on polar surfaces. *Phys Rev Lett* 2003, **91**: 185502.

[23] Geng ZG, Kong XD, Chen WW, *et al*. Oxygen vacancies in ZnO nanosheets enhance CO_2 electrochemical reduction to CO. *Angew Chem Int Ed* 2018, **57**: 6054–6059.

[24] Yuan HY, Aljneibi SAAA, Yuan JR, *et al*. ZnO nanosheets abundant in oxygen vacancies derived from metal-organic frameworks for ppb-level gas sensing. *Adv Mater* 2019, **31**: 1807161.

[25] Yin X, Wang YZ, Chang TH, *et al*. Memristive behavior enabled by amorphous-crystalline 2D oxide heterostructure. *Adv Mater* 2020, **32**: 2000801.

[26] Staemmler V, Fink K, Meyer B, *et al*. Stabilization of polar ZnO surfaces: Validating microscopic models by using CO as a probe molecule. *Phys Rev Lett* 2003, **90**: 106102.

[27] Kong XY, Wang ZL. Polar-surface dominated ZnO nanobelts and the electrostatic energy induced nanohelixes, nanosprings, and nanospirals. *Appl Phys Lett* 2004, **84**: 975–977.

[28] Chen SJ, Liu YC, Shao CL, *et al*. Structural and optical properties of uniform ZnO nanosheets. *Adv Mater* 2005, **17**: 586–590.

[29] Wang J, Ren Y, Liu H, *et al*. Ultrathin 2D $NbWO_6$ perovskite semiconductor based gas sensors with ultrahigh selectivity under low working temperature. *Adv Mater* 2022, **34**: 2104958.